Ultrafast Plasma Electron Dynamics: A Route to Terahertz Pulse Shaping

Sudipta Mondal[1,2,*] Qiliang Wei,[2] Muhammad Ashiq Fareed[2,3] Hassan A. Hafez,[2,4]
Xavier Ropagnol,[2] Shuhui Sun,[2] Subhendu Kahaly[1] and Tsuneyuki Ozaki[2,†]

[1] *ELI-ALPS, ELI-HU Non-Profit Ltd., Dugonics tér 13., Szeged H-6720, Hungary*

[2] *Institut national de la recherche scientifique–Centre Energie Matériaux Télécommunications (INRS-EMT), 1650 Lionel-Boulet, Varennes, Québec J3X 1S2, Canada*

[3] *Chemical Sciences Division, Lawrence Berkeley National Laboratory, Berkeley, California 94720 USA*

[4] *Fakultät für Physik, Universität Bielefeld, Universitätsstr. 25, Bielefeld 33615, Germany*

Intense ultrafast laser interaction with solid-density plasma can lead to relativistic transient electron dynamics that are favorable for the generation of high-field terahertz (THz) pulses. We investigate the temporal characteristics of such THz pulses. Single-shot electro-optic measurements enable us to record the complete temporal profiles of the THz pulses emanating from planar Cu and aligned Cu-nanorod-array plasma. The temporal properties of the THz pulses exhibit several transients. Fully relativistic two-dimensional particle-in-cell simulations corroborate experimental observations and reveal that these features originate from electron microbunch emission from the target. Our results demonstrate that target nanostructuring provides a route to control such ultrafast electron dynamics and hence THz-pulse properties in the time domain.

I. INTRODUCTION

Terahertz (THz) radiation is widely used for imaging [1] and probing of physical systems in broad areas of research, ranging from biology to astrophysics [2–5]. It interacts strongly with various materials, has a unique nonionizing nature, and passes through many media that are opaque to visible radiation, allowing THz radiation to be a safe alternative to x-ray imaging [6]. Intense THz pulses are steadily becoming an essential tool to explore new research areas such as THz nonlinear optics [7,8], single-shot THz spectroscopy and imaging [9], and THz-field-driven streak imaging [10,11]. Such fascinating applications are driving the quest for the development of intense THz sources through the use of several different techniques [12–19].

One such approach that is receiving remarkable attention in THz research is based on relativistic laser-plasma interaction [20–24]. This particular technique holds promise for the generation of near-milljoule- (mJ) level THz-pulse energies with an ultrabroad spectral bandwidth using tabletop-scale laser systems [22,23,25] and would be tested in facilities such as the Extreme Light Infrastructure–Attosecond Light Pulse Source (ELI-ALPS) [26–28]. THz generation from laser-plasma interaction could

benefit further from utilizing micro- and nanostructured targets. Structured-solid plasma targets have already shown their potential in laboratory high-energy-density physics [29], enhancement of high-energy particles [30], and x-ray yield [31,32] and hold promise as ultracompact plasma undulators [33]. The main challenge of high-intensity laser interaction with a nanostructured target is the destruction of nanostructures due to prepulses and pedestals in the high-power laser pulses that interact with the target at different times prior to the main pulse. In spite of the availability of ultrahigh-contrast lasers, nanostructures may be influenced by premature plasma formation in the target. To ensure the survival of the nanostructure, one needs to keep the prepulse intensity sufficiently low and employ time-resolved shadowgraphy, as described by Zhou *et al.* [34], to monitor the interaction.

In recent years, a significant enhancement in the THz energy has been demonstrated while high-intensity laser pulses are interacting with aligned nanorod arrays [23], resulting in THz fields exceeding the MV/cm range when refocused tightly [35]. Such a high-amplitude THz field can provide enormous prospects for THz research. Complete temporal characterization of THz pulses generated from such sources is a prerequisite for their practical applications and is also essential for understanding the phenomena. In addition, detailed investigation of the THz temporal profile could reveal fundamental information on

*sudipta.mondal@eli-alps.hu
†ozaki@emt.inrs.ca

plasma-electron dynamics. However, temporal characterization of THz pulses generated by this technique is challenging, primarily because of the limited target area and the relatively low repetition rate of the high-intensity lasers used in the experiment. Additionally, due to the nonlinear nature of the interaction, intense THz pulses generated in such interactions exhibit large pulse-to-pulse fluctuations resulting from small variations in the laser intensity. This makes single-shot measurement imperative.

In this paper, we report experimental measurements of the temporal profiles of the ultrahigh-peak-field THz pulses generated from plane and nanorod plasmas using single-shot electro-optic (EO) detection. Recorded THz-pulse profiles show that the electromagnetic pulses generated during laser-plasma interaction have several components, including both fast and slow evolution. Finally, we demonstrate that a steering laser parameter or target nanostructuring enables us to control the all-important electron dynamics, which could be a potential avenue for temporal shaping of the THz waveform. To understand the interplay between the complex structures in the measured THz temporal profile and the electron dynamics, we perform two-dimensional (2D) fully relativistic particle-in-cell (PIC) numerical simulations that help us explain the observations qualitatively.

A. Ultrafast electron dynamics

Relativistic electron bunches, both nano- and microbunches, are generated on both sides of a thin target in the interaction with high-intensity femtosecond lasers [36–38]. Electron-nanobunch generation is relevant to high-order-harmonic generation [39], while microbunches are relevant for high-field THz-pulse generation. The dynamics of the electron emission on the front and the rear of the target are substantially different. On the front, electron emission is primarily established by the optical field of the laser [36,40,41].

The physical process of the complex electron-emission dynamics, constructed from PIC-simulation results, is as follows. High-energy electron jets are generated during the initial stages of the interaction and build up an electrostatic potential near the front surface of the target. Electrons with very high energy are able to escape through this electrostatic potential, while lower-energy electrons in the vicinity of the target surface reflect back and interact with the target again to generate secondary electrons and form an electron cloud. This process plays a significant role in determining the properties of high-energy electron bunches emitted at later times. A large portion of the high-energy electrons propagates into the target and is emitted from the rear surface and eventually builds up a sheath potential at the rear, which quickly becomes sufficiently strong to reflect electrons toward the front of the target; electron emission from the front then takes place again.

This refluxing of the electrons inside the target continues and electron bunches are emitted repeatedly at later times [42]. Hence, the typical time duration of electron bunches generated in the interaction with high-intensity femtosecond laser pulses is often in the range of several picoseconds [37,38]. Experimental charge-dynamics measurements by Pompili *et al.* indicate the existence of several electron bunches generated in the interaction [37].

B. Intense THz-pulse generation

THz-pulse generation in high-intensity femtosecond laser interaction with solid-density plasma can be correlated with fast electron currents or the collective dynamics of the electrons. To be precise, these THz pulses are generated by means of coherent-transition radiation (CTR), when energetic electrons that are generated in the interaction pass through a plasma-vacuum boundary [23,43,44]. Simple calculations by Schroeder *et al.* have shown that the total energy generated in the CTR over all angles and frequencies is given by [45]

$$W_{\text{tot}} \simeq 4 r_e m_e c^2 N^2 \ln(\gamma)/\lambda_{\text{min}}, \tag{1}$$

$$W_{\text{tot}}[J] \simeq 3.6 \times 10^{-2} (Q[nC])^2 ln(\gamma)/\lambda_{\text{min}}, \tag{2}$$

where λ_{min} is the minimum wavelength for which the condition for CTR is satisfied—which depends on the electron-bunch dimensions—r_e, m_e, c, N, Q, and γ are the classical radius of the electron, the electron's rest mass, the speed of light, the number of electrons, the total charge of the electron bunch in units of nanocoulombs (nC), and the Lorentz factor ($\gamma = 1/\sqrt{1 - v^2/c^2}$), respectively. For a crude estimation, let us consider an electron bunch consisting of charge $Q = 1$ nC (a typical value generated in high-intensity laser-plasma interactions on solid-density targets [46]) of relativistic electrons moving with speed $v = 0.99c \Rightarrow \gamma \simeq 7$. The total estimated CTR energy generated up to the frequency 20 THz ($\lambda_{\text{min}} = 15 \ \mu$m) is nearly 4.6 mJ over all emission angles. Such a large amount of THz-pulse energy drives the research on plasma-based THz sources. The characteristics of the THz pulses generated by the electron bunches via CTR largely depend on the properties of those electron bunches. Further, the temporal profile of the THz pulses contains signatures of all the electron bunches emitted at different times.

II. EXPERIMENTAL RESULTS AND DISCUSSIONS

A. Experimental setup

EO sampling is a widely used technique to measure the temporal profile of the THz electric field. Being a scanning technique, it requires a large number of laser shots to acquire a complete trace of the THz waveform [3,47–49]. The low pulse-to-pulse stability of high-power

lasers limits the use of conventional EO sampling measurements and hence the scanning version cannot be employed directly for laser-plasma-based THz sources [8]. To overcome these difficulties, we use single-shot EO sampling for the temporal characterization of the THz electric field, similar to that described by Minami *et al.* [50]. Several single-shot THz detection schemes have been demonstrated with different experimental geometries [50–52]. While a noncollinear geometry provides continuous temporal information, a collinear geometry is easy to establish on a single-shot basis [8]. Figure 1(a) shows a schematic diagram of the experimental setup used for single-shot EO THz detection. The experiments are performed using the 10-Hz beamline of the Advanced Laser Light Source (ALLS) at the Institut national de la recherche scientifique–Centre Energie Matériaux Télécommunications (INRS-EMT). This beamline can deliver a maximum 350 mJ of laser energy before compression at an 800-nm central wavelength and with a nanosecond temporal contrast better than 2×10^{-7}. After compression, it can produce 240 mJ of laser energy on the target for a duration of 40 fs. The laser is then focused on a polished Cu (dimensions 5 cm $\times$ 5 cm $\times$ 3 mm) or an aligned Cu-nanorod-array target (nanorod dimensions: diameter 200 nm, with various lengths) over a spot of diameter approximately 20 μm at an angle of $45°$ with respect to the target normal by using an $f/3$ off-axis parabolic mirror. As a result, a maximum intensity of 3.5×10^{18} W/cm^2 is achieved on the target. The target is mounted on a computer-controlled *XYZ* translation stage placed inside the vacuum chamber, so that each laser shot interacts with a fresh target surface, thus maintaining identical experimental conditions. THz pulses emitted in the specular direction are then collimated and guided out of the vacuum chamber by using thick gold-coated off-axis parabolic and flat mirrors through an ultrahigh-molecular-weight polyethylene (UHMWPE) window, which also acts as a low-pass filter and transmits radiation below 20 THz. All higher-frequency radiation is blocked. Any trace of visible and near-infrared electromagnetic radiation, if they are present, is blocked by the use of a high-resistivity float-zone silicon filter. The transmitted THz radiation is then refocused by another gold-coated off-axis parabolic mirror onto an EO crystal (ZnTe) and is used for THz detection.

A part of the main laser beam (< 1 mJ) is extracted after compression and reduced in diameter by means of a beam reducer, which is then used as the probe pulse. The temporal delay in the probe is introduced by a reflective echelon mirror (E), as shown in Fig. 1(a). The echelon mirror (size 10 mm $\times$ 10 mm) is made of polished nickel with 500 steps of height 5 μm and width 20 μm and is placed just before the interaction with the THz pulses. The basic principle of the echelon mirror is explained in Fig. 1(b). A laser pulse reflected from the echelon mirror is divided into 500 beamlets, as shown in Fig. 1(b), with a temporal
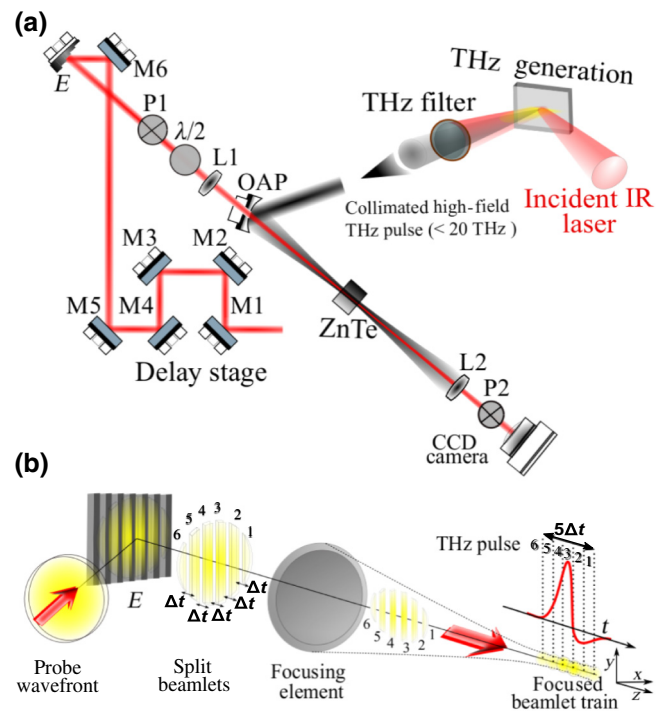

FIG. 1. (a) A schematic diagram of the experimental setup used for single-shot electro-optic detection. THz pulses are generated by high-intensity laser-plasma interaction on a Cu target. An echelon mirror (E) is used to replace the temporal delay line required in an EO-sampling experiment. (b) The echelon mirror (E) consists of several steps and splits a plane wave front into several beamlets with a delay (Δt) between the beamlets. It finally generates a train of beamlets at the focus, which interact with the THz pulse inside the ZnTe crystal to capture its temporal profile in a single shot.

delay ($\Delta t \approx 35$ fs) between the beamlets that is sufficient to record a complete THz field profile with acceptable resolution. The temporal delay (Δt) is determined by the step height of the echelon mirror. The probe is focused onto the EO crystal (ZnTe), through a central hole in the off-axis parabolic mirror, and its time-delayed beamlets overlap coaxially with the THz pulse and are mapped onto the CCD camera, as shown in Fig. 1(a).

The spectral sensitivity of the single-shot EO setup is determined mainly by a 1-mm-thick ZnTe crystal, which has a cutoff at 4 THz. The THz pulses from the planar Cu target as well as aligned nanorod targets are characterized in the setup and are discussed in Sec. II C.

B. Cu-nanorod target preparation

The Cu-nanorod target preparation is based on the anodic aluminum oxide (AAO) template method as described in Ref. [23]. Briefly, a gold layer is sputtered on one side of the through-hole AAO template (a Whatman® Anodisc with a pore diameter of 200 nm and a height of

60 μm) and is used as the working electrode in a three-electrode cell, while a graphite-carbon plate and saturated calomel electrode (SCE) serve as the counter and reference electrodes, respectively. The electrolyte is 0.2 M $CuSO_4 \cdot 5H_2O + 0.1$ M H_3BO_3 for Cu-nanorod deposition. Experiments are carried out under a constant potential of -1.20 V (vs SCE) at room temperature. The length of the Cu nanorods can be controlled by adjusting the deposition time. Prepared Cu nanorods embedded in AAO template are first pasted on a thick Cu target and then immersed in the NaOH solution to dissolve the alumina membrane. Then, the nanorods are rinsed thoroughly with distilled water and ethyl alcohol several times before undergoing a SEM characterization and eventually the THz experiment.

Figure 2 shows SEM images of a nanorod target with a length of 10 μm with two different magnifications. It is evident from the SEM images that a large number of well-aligned Cu nanorods are successfully fabricated via this technique. The Cu nanorods are dense and homogeneous in diameter and are parallel to each other. The diameter of the Cu nanorods is approximately 200 nm, which is consistent with the pore diameter of the AAO template used in nanorod fabrication.

C. Results and discussion

Figures 3(a)–3(f) show the THz field calculated from the CCD images recorded in the experiment for three different conditions. For Figs. 3(a)–3(c), we crop a rectangular area of size 30 pixels in width and 400 pixels in length from the background-corrected probe images recorded in the experiment. The signal recorded in each pixel of the cropped probe image is then converted to a THz field (spatiotemporal profile of THz pulses). Due to large pulse-to-pulse fluctuations and the complex spatial profile of the probe beam, the averaged THz temporal waveform suppresses the microscopic details about the temporal profile; hence we prefer to present the spatiotemporal profile [as shown in Figs. 3(a)–3(c)] of the THz pulse for a better understanding. The averaged (integrated over space) THz temporal profile is also shown in Figs. 3(d)–3(f).

Figures 3(a) and 3(d) show the temporal profile of the THz field for varying driver-laser intensities. The laser

intensity is varied by adjusting the laser energy using a combination of a half-wave plate and a thin-film polarizer placed inside the laser system before the final amplifier. A wide negative region with a temporal width of at least 2.3 ps [clearly visible in Fig. 3(a)] is observed at lower laser intensities. In several THz profiles, this negative region is wider than 3 ps. As the laser intensity increases, sharp THz peaks with notably shorter durations (100–300 fs) start to grow inside the wide negative region and dominate at higher laser intensities. Finally, the longer negative region becomes less pronounced due to the large amplitude of the sharp peaks. This feature is observed at intensities of 2.4×10^{18} W/cm^2 and 2.7×10^{18} W/cm^2 in Fig. 3(a).

Suitable target structuring provides control over hot-electron generation and the electron emission dynamics. This emission dynamics then reshapes the temporal waveform of the THz pulses. Target nanostructuring is one such method, which has been used in several areas in laser-plasma interaction. Hence aligned Cu-nanorod-array targets are used in this experiment to demonstrate the control over the temporal waveform of the THz pulses. Figure 3(b) shows the THz field profile obtained in the single-shot EO THz detection experiment with aligned nanorod targets of different lengths, ranging from 1 μm to 30 μm at a laser intensity of 8×10^{17} W/cm^2. Two visibly distinct components (the slow and fast component) are observed in the THz profile.

These THz field profiles show that the THz pulses are comprised of a wide peak corresponding to the negative component of the electric field (blue area) with a relatively long duration (slow component) for all targets. However, this component is prominent for the case of the planar target in Fig. 3(a) and the 1-μm- and 2-μm-long nanorod targets in Fig. 3(b). The width of this negative region is ≥ 2.3 ps. As the nanorod length is increased, multiple sharp peaks with a shorter duration (fast components) start to become visible inside this negative region. The number of sharp peak increases with the nanorod length.

The typical multipeak nature of the THz waveform from the aligned nanorod target is absent at higher laser intensity (3.5×10^{18} W/cm^2), as shown in Fig. 3(c). In this case, mainly a high-amplitude shorter-duration positive peak followed by a wider negative region is observed.
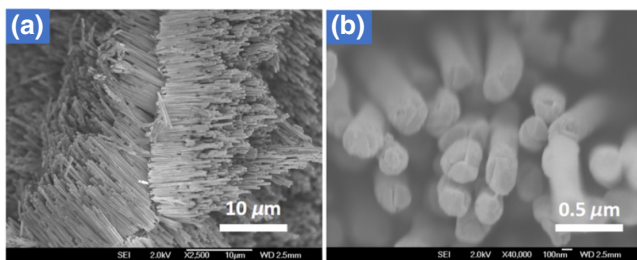
III. PARTICLE-IN-CELL SIMULATION

In order to understand the generation of high-field THz pulses and its correlation with the electron dynamics that ensue in such interactions, we perform a series of 2D PIC simulations with the fully relativistic code PICCANTE [53], under our relevant experimental conditions. The PIC-simulation geometry is shown in Fig. 4(a). A spatially and temporally Gaussian laser pulse with a full-width-at-half-maximum (FWHM) pulse duration of 40 fs and polarization in the plane of incidence impinges at a 45° angle

FIG. 2. SEM images of Cu nanorod arrays at different magnifications: (a) cross-section view; (b) top view.
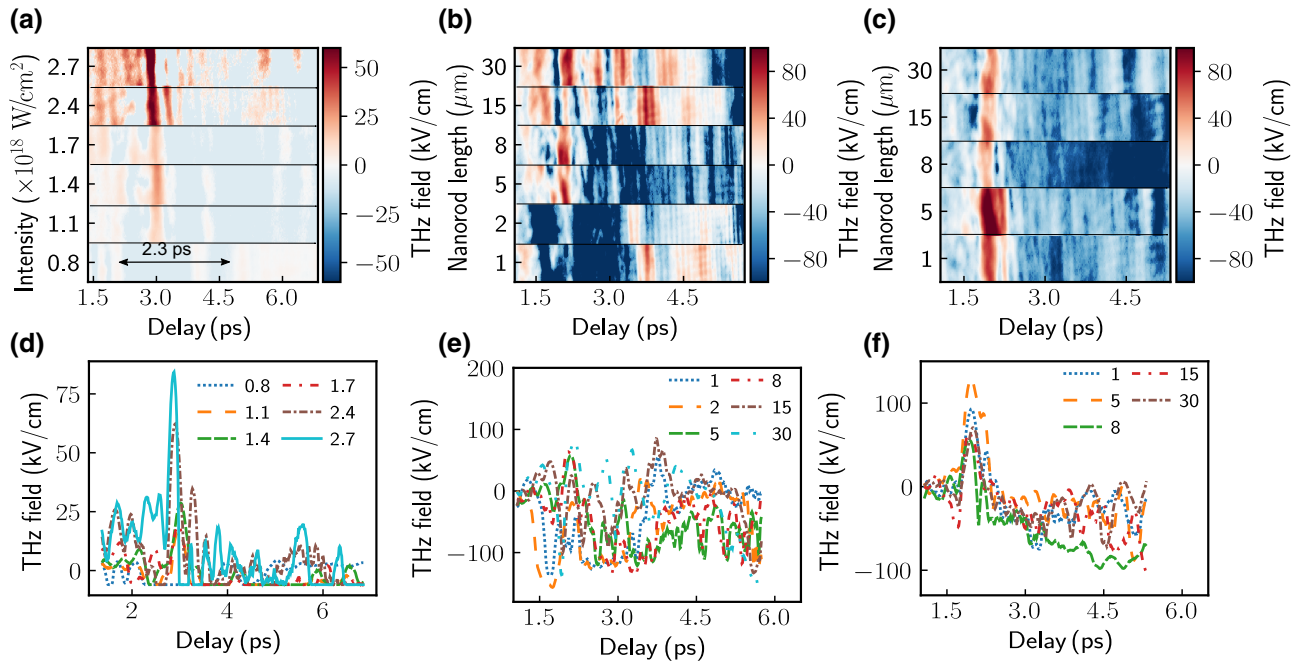
FIG. 3. (a) The experimentally recorded THz field generated from a plane Cu target as a function of the driver-laser intensity. (b),(c) The THz field generated from an aligned nanorod target of diameter 200 nm with various lengths at laser intensity (b) 8×10^{17} W/cm^2 and (c) 3.5×10^{18} W/cm^2. The THz field is calculated for each pixel of a resized probe image of size 30×400 pixels for a better grasp on the spatiotemporal distribution of the THz field. (d)–(f) The average THz field profiles generated from the spatiotemporal profiles of the THz field in (a)–(c), respectively. The numbers in the legend in (d) represent the laser intensity in 10^{18} W/cm^2, whereas the numbers in the legends in (e) and (f) represent the nanorod length in micrometers.

on a 12-μm-thick Cu target. Although the experiments are performed with a 3-mm-thick Cu target, the simulations are performed using thin targets (12 μm) to reduce the computational requirements, since the target size and the characteristic time in the experiment are much larger than any PIC code would accept. Ideally, one needs to perform a combination of hydrodynamic, PIC, and Monte Carlo N-particle transport codes for exact reproduction of the experimental data [54]. However, these simulations are computationally expensive, while PIC simulations are fairly sufficient to understand the overall features of the THz temporal profile and the role of electron recirculation inside the target on the macroscopic structures of the THz waveform.

In typical simulations, we use singly ionized Cu plasma with an exponential density profile given by $n_e = n_0 \exp(-x/L)$ where L is the density scale length and n_0 is the maximum plasma electron density, which is set to $10n_c$, n_c being the critical plasma density. A normalized laser amplitude of $a_0 = 2$ ($a_0 = 8.53 \times 10^{-10} \times (I\lambda^2)^{1/2}$, where I is the laser peak intensity in W/cm^2 and $\lambda = 0.8$ μm is the central wavelength) is used throughout the simulations. The simulation box of size $140\lambda \times 140\lambda$ is divided into 3000×3000 cells. We use 100 electrons and 100 ions in each cell. The interaction time ($t = 0$) is set to the moment at which the peak of the driving laser

pulse interacts with the target. Figures 4(b)–4(f) show the evolution of the low-frequency magnetic field (B_z) after the interaction. The high-frequency B_z component of the driving laser is filtered out using a suitable low-pass FFT filter. Figures 4(b)–4(f) also demonstrate that the THz emission is highly anisotropic and that most of the THz energy is emitted long after the interaction with the main pulse.
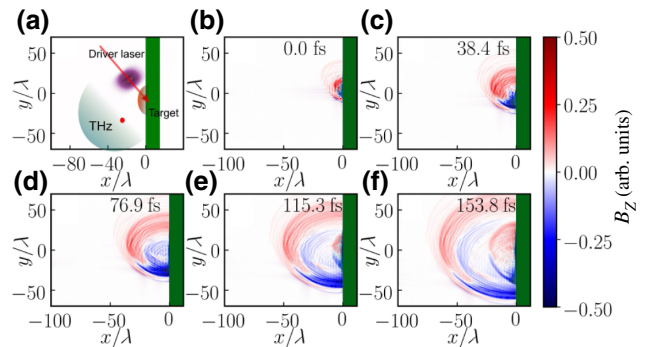

FIG. 4. (a) The simulation geometry. The red dot represents the position of the numerical probe. (b)–(f) The magnetic field (B_z) distribution on the front of the target obtained from PIC simulation at different times after the interaction. The driver laser is filtered out using a spectral filter based on fast Fourier transformation.

An in-depth observation reveals the presence of several periodic structures in the B_z-field profile.

In order to further analyze the temporal waveform, a numerical probe of size 0.25λ is set at 30λ before the target to collect THz radiation in the specular direction. The red dot in Fig. 4(a) represents the probe position. A scan through the temporal series of magnetic field snaps provides the temporal profile of the THz field (≤ 15 THz) and is shown in Fig. 5(a) for plain targets of different thicknesses. The numbers in the legend represent the thicknesses of the plane target. A low-pass Butterworth filter is applied to extract the contribution of $B_z(t)$ below 15 THz. The complex temporal profile shows several periodic structures with one small positive peak, followed by a broad negative dip with several smaller peaks inside the broader negative dip, similar to the experimental data, and is shown in Fig. 3. The smaller peaks inside the negative dip shift to a later time for thicker targets. These microscopic features of the THz temporal profile can be linked to the current dynamics inside the target and are described later in the paper.

To understand the role of the electron-emission dynamics on THz generation, the time-dependent electron spectrum is analyzed and plotted in Figs. 5(b) and 5(c). Figure 5(b) shows the time-dependent energy spectrum of the electrons detected between 0.5λ and 1λ at the front of the target, whereas Fig. 5(c) shows the time-dependent angular spectrum of the electrons at the front of the target. The color axis represents the numbers of electrons, in arbitrary units. Figures 5(b) and 5(c) reveal that relativistic energy electrons are emitted over several hundreds of femtoseconds after the interaction and, more interestingly, that the electrons are emitted in several microbunches. In our case, the electrons are emitted in four different microbunches. Thorough investigation of the fundamental filtered magnetic field snapshots [Figs. 4(b)–4(f)] reveals

that the microscopic structures (each semicircle) in the magnetic field images in Figs. 4(b)–4(f) and in the temporal profile in Fig. 5(a) are generated at the time instant at which an electron microbunch is emitted from the target surface.

Figure 5(c) also unveils the angular distribution of each electron microbunch. The first electron microbunch is generated at an early stage of the interaction, while the driver laser is still interacting with the target, and it is highly anisotropic. This electron bunch is mostly emitted in the specular-reflection direction. Consequently, the THz radiation (or CTR) generated by this electron microbunch is highly anisotropic and is evident from Figs. 4(b)–4(f). The electron microbunches slowly become isotropic at later times [after 300 fs in Fig. 5(c)] and hence so do the THz pulses. In the event that the electrons are emitted normal to the target, CTR is generated into a narrow cone close to the target surface and the radiated energy (W_e) per unit frequency (ω), per unit solid angle (Ω), is given by [45]

$$\frac{d^2 W_e}{d\omega d\Omega} = \frac{r_e m_e c}{\pi^2} \frac{\beta^2 \gamma^4 \theta^2}{(1 + \beta^2 \gamma^2 \theta^2)^2}, \qquad (3)$$

where θ is the observation angle with respect to the electron trajectory and $\beta = v/c$ is the velocity of the electron normalized by the speed of light, c. Each electron microbunch in Fig. 5(c) exhibits a slightly different angular distribution and, finally, the fourth electron bunch is emitted perpendicular to the target. Consequently, this electron-emission behavior is reflected in the angular distribution of $B_z(t)$ in Figs. 6(a)–6(c), which show the angular distribution of the THz temporal waveform from plane targets of different thicknesses, as shown in Figs. 6(a) for a 10λ-thick target, 6(b) for a 15λ-thick target, and 6(c) for a 20λ-thick target, respectively.

The delay between the emission of two successive electron microbunches from the target is approximately equal to the electron recirculation time inside the target. The recirculation time (T_{recirc}) depends on the target thickness (L) and the recirculation speed (v_e) of the electron currents inside the target and is given by $T_{\text{recirc}} \sim 2L/v_e$.
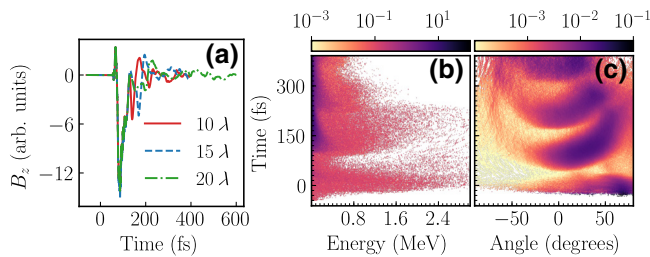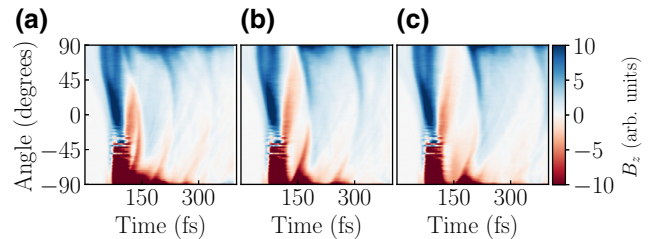

FIG. 5. (a) The temporal profile of the THz field generated in PIC simulation from plane targets of different thicknesses. A low-pass Butterworth filter is applied to extract the THz field in the frequency range ≤ 15 THz. (b) The electron energy spectrum from simulation as a function of the interaction time detected between 0.5λ and 1λ in front of the target. The color axis represents dN/dE, in arbitrary units. (c) The angular spectrum from simulation as a function of the interaction time. The color axis represents $dN/d\theta$, in arbitrary units.

FIG. 6. The angular distribution of the THz waveform generated in PIC simulation for three different target thicknesses: (a) 10λ, (b) 15λ, and (c) 20λ. A low-pass Butterworth filter is applied to extract spectral components ≤ 15 THz.

The electron recirculation time increases with the target thickness for fixed laser and plasma parameters [42]. This behavior is observed in Figs. 6(a)–6(c). The delay between the peaks in the THz waveform increases with the target thickness due to a longer electron recirculation time for a thicker target.

The first peak is relatively strong, whereas the peaks at later times are weaker. In addition, the $B_z(t)$ emitted by the first electron microbunch [first peak in Figs. 6(a)–6(c)] is highly anisotropic, as the first electron bunch is emitted in the specular-reflection direction [Fig. 5(c)]. On the other hand, the $B_z(t)$ emitted by the electron microbunches at later times [peaks at later times in Figs. 6(a)–6(c)] slowly becomes isotropic and is consistent with the angular electron spectrum shown in Fig. 5(c).

In Figs. 7(a)–7(f), we plot the electron density during and after the interaction. The color axis represents the electron density normalized to the critical electron density. A large number of electron ejections are observed before 32 fs, 109 fs, and 238 fs, whereas the electron ejection during the intermediate time is significantly reduced. The electron ejection time is consistent with the peaks in the THz waveform. Further, the electron bunches in Figs. 7(a), 7(c), and 7(e) are emitted at different angles.

Figures 8(a)–8(f) show the electron phase space (P_x/m_ec-x) at six different simulation times (the same times as in Fig. 7), which reconfirms the electron recirculation inside the target after the interaction. The recirculation time depends on the thickness of the plasma. In the 15λ-thick plasma, the recirculation time is nearly 103 fs, with an average electron recirculation speed inside the target of approximately 2.3×10^8 m/s.

FIG. 8. The electron phase space (P_x/m_ec-x) from PIC simulation at six different times after the interaction shows electron recirculation. The dotted lines mark the positions of the target surfaces.

IV. WAVEFORM SHAPING OF THz PULSES

The electron-microbunch emission can be adjusted to a considerable extent by tuning the laser and plasma parameters. In this paper, we experimentally demonstrate two simple cases in which the laser [Fig. 3(a)] and the plasma parameters [Figs. 3(b) and 3(c)] are adjusted to shape the THz waveform in the time domain (Sec. III). In the first case, we vary the intensity of the driving laser for this purpose, while in the second case we use an aligned Cu-nanorod-array target. The 2D PIC-simulation results also reconfirm that these two approaches can satisfactorily shape the THz waveform in the time domain.

THz field profiles from PIC simulation for three different laser intensities are shown in Fig. 9(a). The legend numbers in Fig. 9(a) represent the driver-laser intensity in units of 10^{18} W/cm^2. As the driving laser intensity increases, besides increasing the THz intensity, more structures appear in the THz field profile. At lower laser intensity (0.77×10^{18} W/cm^2), the large negative dip (first dip) is substantially reduced and structures generated by the recirculation of the electron currents are comparable with
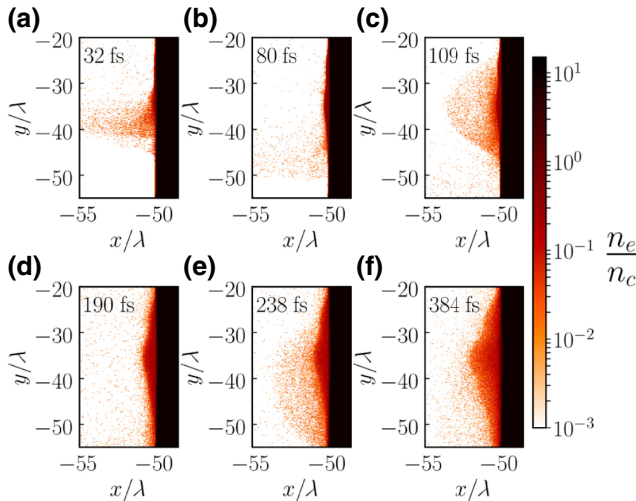

FIG. 7. The evolution of the electron density (normalized to the critical density) in PIC simulation, at different times. A large number of electron ejections from the target are observed at times of 32 fs, 109 fs, and 238 fs after the interaction. However, in the intermediate time intervals, the electron ejection is significantly reduced.
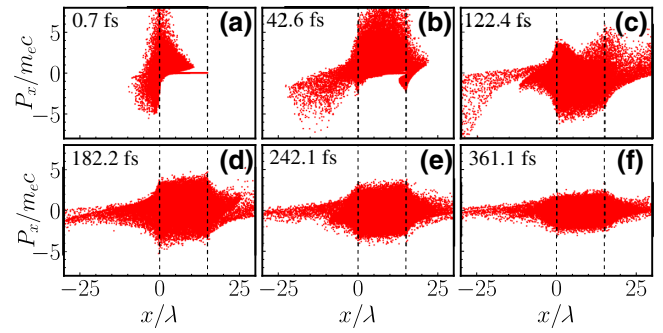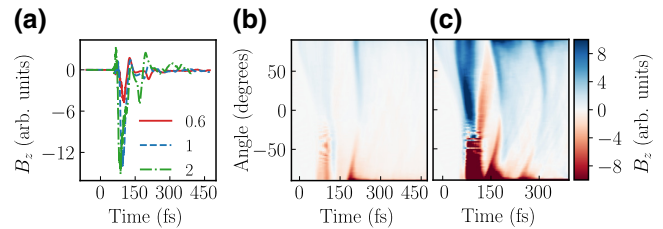

FIG. 9. (a) The temporal profile of the THz pulses at three different laser intensities recorded in PIC simulation in the specular-reflection direction. The numbers in the legend represent the driver-laser intensity in units of 10^{18} W/cm^2. The angular distribution of the time-dependent THz field generated from PIC simulation at the driver-laser intensities (b) 0.77×10^{18} W/cm^2 and (c) 8.58×10^{18} W/cm^2.
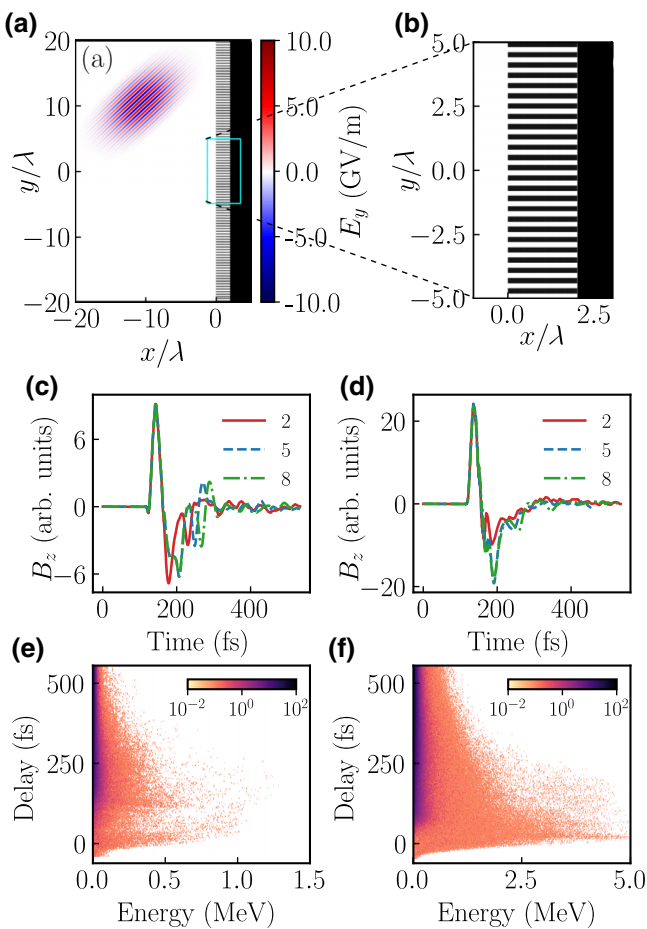
FIG. 10.　(a) The simulation geometry for the nanorod target. (b) An enlargement of the target, to show the aligned nanorod target on the planar surface. The THz waveform generated from the nanorod target in the specular-reflection direction at laser intensity (c) 0.77×10^{18} W/cm^2 and (d) 8.58×10^{18} W/cm^2, using 2D PIC simulation. The numbers in the legend represent the nanorod length in micrometers. (e),(f) The time-resolved electron spectrum from a 5-μm-long nanorod target at two different laser intensities, 0.77×10^{18} W/cm^2 and 8.58×10^{18} W/cm^2, respectively, obtained from simulation. The color axis represents dN/dE, in arbitrary units.

the large negative peak. On the other hand, at higher laser intensity (2.14×10^{18} W/cm^2), the first negative dip is substantially larger and dominant.

In another case, we use aligned Cu-nanorod-array targets for plasma shaping to alter the interaction. The experimental results are shown in Figs. 3(b) and 3(c).

In order to understand the effect of the aligned Cu-nanorod-array targets on THz generation, we perform several 2D PIC simulations with targets that resemble an aligned-nanorod-array target in two dimensions. The simulation geometry is shown in Fig. 10(a). All other simulation parameters are identical to those of the plane target. The nanorods, of diameter 200 nm and of varying lengths, are

aligned normally on a plane target surface. The spacing between nanorods remains fixed at 200 nm, as shown in Fig. 10(b).

Figures 10(c) and 10(d) show the THz waveform for nanorod targets of varying nanorod lengths and for two different laser intensities: 0.77×10^{18} W/cm^2 and 8.58×10^{18} W/cm^2. At lower laser intensity (0.77×10^{18} W/cm^2), the THz waveform consists of a large positive peak followed by a wide negative region and several structures in the wide negative region, similar to Fig. 3(b). However, at a higher laser intensity (8.58×10^{18} W/cm^2), the THz waveform generated from the nanorod target is relatively smoother and is composed of one large positive peak and one wider negative dip, which is consistent with the experimental data, as shown in Fig. 3(c).

To understand the THz waveform from the nanorod target, we plot the time-resolved electron spectrum, which is detected between 0.5λ and 1λ in front of the target, from a 5-μm-long nanorod target, in Figs. 10(e) and 10(f), respectively. Figure 10(e) shows the time-resolved electron spectrum at laser intensity 0.77×10^{18} W/cm^2, whereas Fig. 10(f) shows the electron spectrum at 8.58×10^{18} W/cm^2. The color axis represents electron macroparticle number, in arbitrary units. In comparison with the electron spectrum shown in Fig. 5(b) from the plane target, the electron spectrum from the aligned nanorod target [Figs. 10(e) and 10(f)] is smoother. Consequently, the THz waveforms are also smoother. However, at lower laser intensity [0.77×10^{18} W/cm^2; Fig. 10(e)], the time-resolved electron spectrum still exhibits electron-microbunch emission, although is not as prominent as for the case of the planar target. The smoother THz waveform from the nanorod target [shown in Fig. 10(d)] at higher laser intensity (8.58×10^{18} W/cm^2) results from continuous emission of electrons from the target, which is shown in Fig. 10(f).

V. CONCLUSIONS

The temporal characteristics of high-field THz pulses generated by the interaction of high-intensity lasers with a plane and an aligned-nanorod-array target are investigated experimentally and reproduced by PIC simulations. A strong correlation is found between the high-field THz pulse and relativistic electron-microbunch emission. The PIC-simulation results show that the temporal profile of the THz pulses carries information about different electron microbunches emitted from the target at different times. The time evolution of the THz fields shows a sharp positive peak followed by a wide valley, corresponding to a negative electric field component of the THz pulses with a longer temporal duration (≥ 2.3 ps). By tuning the laser and plasma parameters, the THz waveform can be shaped in the temporal domain.

ACKNOWLEDGMENTS

[1] Wai Lam Chan, Jason Deibel, and Daniel M. Mittleman, Imaging with terahertz radiation, Rep. Prog. Phys. 70, 1325 (2007).

[2] Ronald Ulbricht, Euan Hendry, Jie Shan, Tony F. Heinz, and Mischa Bonn, Carrier dynamics in semiconductors studied with time-resolved terahertz spectroscopy, Rev. Mod. Phys. 83, 543 (2011).

[3] Lee Yun-Shik, *Principles of Terahertz Science and Technology* (Springer Science and Business Media, New York, 2009).

[4] P. U. Jepsen, D. G. Cooke, and M. Koch, Terahertz spectroscopy and imaging—Modern techniques and applications, Laser Photon. Rev. 5, 124 (2011).

[5] Tobias Kampfrath, Koichiro Tanaka, and Keith A. Nelson, Resonant and nonresonant control over matter and light by intense terahertz transients, Nat. Photonics 7, 680 (2013).

[6] John F. Federici, Brian Schulkin, Feng Huang, Dale Gary, Robert Barat, Filipe Oliveira, and David Zimdars, THz imaging and sensing for security applications—explosives, weapons and drugs, Semicond. Sci. Technol. 20, S266 (2005).

[7] Hassan A. Hafez, Ibraheem Al-Naib, Marc M. Dignam, Yoshiaki Sekine, Katsuya Oguri, François Blanchard, David G. Cooke, Satoru Tanaka, Fumio Komori, Hiroki Hibino, and Tsuneyuki Ozaki, Nonlinear terahertz field-induced carrier dynamics in photoexcited epitaxial monolayer graphene, Phys. Rev. B. 91, 035422 (2015).

[8] H. A. Hafez, X. Chai, A. Ibrahim, S. Mondal, D. Férachou, X. Ropagnol, and T. Ozaki, Intense terahertz radiation and their applications, J. Opt. 18, 093004 (2016).

[9] Kai-Erik Peiponen, Axel Zeitler, and Makoto Kuwata-Gonokami, eds., *Terahertz Spectroscopy and Imaging*, Springer Series in Optical Sciences Vol. 171 (Springer, Berlin, 2013).

[10] U. Frühling, M. Wieland, and M. Gensch, Single-shot terahertz-field-driven x-ray streak camera, Nat. Photonics 3, 523 (2009).

[11] Lingrong Zhao *et al.*, Terahertz Streaking of Few-Femtosecond Relativistic Electron Beams, Phys. Rev. X 8, 021061 (2018).

[12] József A. Fülöp, Gyula Polónyi, Balazs Monoszlai, Giedrius Andriukaitis, T. Balciunas, Audrius Pugzlys, Graham Arthur, Andrius Baltuska, and Janos Hebling, Highly efficient scalable monolithic semiconductor terahertz pulse source, Optica 3, 1075 (2016).

[13] H. Hirori, A. Doi, F. Blanchard, and K. Tanaka, Single-cycle terahertz pulses with amplitudes exceeding 1 MV/cm generated by optical rectification in LiNbO$_3$, Appl. Phys. Lett. 98, 091106 (2011).

[14] Mostafa Shalaby and Christoph P. Hauri, Demonstration of a low-frequency three-dimensional terahertz bullet with extreme brightness, Nat. Commun. 6, 5976 (2015).

[15] T. I. Oh, Y. S. You, N. Jhajj, E. W. Rosenthal, H. M. Milchberg, and K. Y. Kim, Intense terahertz generation in two-color laser filamentation: Energy scaling with terawatt laser systems, New J. Phys. 15, 075002 (2013).

[16] X. Ropagnol, M. Khorasaninejad, M. Raeiszadeh, S. Safavi-Naeini, M. Bouvier, C. Y. Côté, A. Laramée, M. Reid, M. A. Gauthier, and T. Ozaki, Intense THz pulses with large ponderomotive potential generated from large aperture photoconductive antennas, Opt. Express 24, 11299 (2016).

[17] Matteo Clerici, Marco Peccianti, Bruno E. Schmidt, Lucia Caspani, Mostafa Shalaby, Mathieu Giguère, Antonio Lotti, Arnaud Couairon, François Légaré, Tsuneyuki Ozaki, Daniele Faccio, and Roberto Morandotti, Wavelength Scaling of Terahertz Generation by Gas Ionization, Phys. Rev. Lett. 110, 253901 (2013).

[18] Ye Tian, Jiansheng Liu, Yafeng Bai, Shiyi Zhou, Haiyi Sun, Weiwei Liu, Jiayu Zhao, Ruxin Lii, and Zhizhan Xux, Femtosecond-laser-driven wire-guided helical undulator for intense terahertz radiation, Nat. Photonics 11, 242 (2017).

[19] Indranuj Dey, Kamalesh Jana, Vladimir Yu Fedorov, Anastasios D. Koulouklidis, Angana Mondal, Moniruzzaman Shaikh, Deep Sarkar, Amit D. Lad, Stelios Tzortzakis, Arnaud Couairon, and G. Ravindra Kumar, Highly efficient broadband terahertz generation from ultrashort laser filamentation in liquids, Nat. Commun. 8, 1184 (2017).

[20] Zheng-Ming Sheng, Kunioki Mima, Jie Zhang, and Heiji Sanuki, Emission of Electromagnetic Pulses from Laser Wakefields through Linear Mode Conversion, Phys. Rev. Lett. 94, 095003 (2005).

[21] G. Q. Liao *et al.*, Bursts of Terahertz Radiation from Large-Scale Plasmas Irradiated by Relativistic Picosecond Laser Pulses, Phys. Rev. Lett. 114, 255001 (2015).

[22] A. Gopal, S. Herzer, A. Schmidt, P. Singh, A. Reinhard, W. Ziegler, D. Brömmel, A. Karmakar, P. Gibbon, U. Dillner, T. May, H-G. Meyer, and G. G. Paulus, Observation of Gigawatt-Class THz Pulses from a Compact Laser-Driven Particle Accelerator, Phys. Rev. Lett. 111, 074802 (2013).

[23] S. Mondal, Q. Wei, W. J. Ding, H. A. Hafez, M. A. Fareed, A Laramée, X Ropagnol, G. Zhang, S. Sun, Z. M. Sheng, J. Zhang, and T. Ozaki, Aligned copper nanorod arrays for highly efficient generation of intense ultra-broadband THz pulses, Sci. Rep. 7, 40058 (2017).

[24] S. Mondal, Q. Wei, S. Kahaly, H. A. Hafez, F. Sylla, X. Ropagnol, M. A. Fareed, S. Sun, and T. Ozaki, in *2017 Conf. Lasers Electro-Optics Eur. Eur. Quantum Electron. Conf.* (IEEE, Munich, Germany, 2017), p. 1.

[25] Guoqian Liao, Yutong Li Hao Liu, Graeme G. Scott, David Neely, Yihang Zhang, Baojun Zhu, Zhe Zhang, Chris Armstrong, Egle Zemaityte, Philip Bradford, Peter G. Huggard, Dean R. Rusby, Paul McKenna, Ceri M. Brenner, Nigel C. Woolsey, Weimin Wang, Zhengming Sheng, and Jie Zhang,

Multimillijoule coherent terahertz bursts from picosecond laser-irradiated metal foils, Proc. Natl. Acad. Sci. **116,** 3994 (2019).

[26] Sudipta Mondal, Mojtaba Shirozhan, Naveed Ahmed, Maïmouna Bocoum, Frederik Boehle, Aline Vernier, Stefan Haessler, Rodrigo Lopez-Martens, François Sylla, Cedric Sire, Fabien Quéré, Kwinten Nelissen, Katalin Varjú, Dimitris Charalambidis, and Subhendu Kahaly, Surface plasma attosource beamlines at ELI-ALPS, J. Opt. Soc. Am. B **35,** A93 (2018).

[27] Sergei Kühn *et al.*, The ELI-ALPS facility: The next generation of attosecond sources, J. Phys. B: At., Mol. Opt. Phys. **50,** 132002 (2017).

[28] Dimitris Charalambidis *et al.*, in *Progress in Ultrafast Intense Laser Science XIII, Springer Series in Chemical Physics*, edited by K. Yamanouch (Springer, Cham, 2017), p. 181.

[29] Clayton Bargsten, Reed Hollinger, Maria Gabriela Capeluto, Vural Kaymak, Alexander Pukhov, Shoujun Wang, Alex Rockwood, Yong Wang, David Keiss, Riccardo Tommasini, Richard London, Jaebum Park, Michel Busquet, Marcel Klapisch, Vyacheslav N. Shlyaptsev, and Jorge J. Rocca, Energy penetration into arrays of aligned nanowires irradiated with relativistic intensities: Scaling to terabar pressures, Sci. Adv. **3,** e1601558 (2017).

[30] Dimitri Khaghani, Mathieu Lobet, Björn Borm, Loïc Burr, Felix Gärtner, Laurent Gremillet, Liana Movsesyan, Olga Rosmej, Maria Eugenia Toimil-Molares, Florian Wagner, and Paul Neumayer, Enhancing laser-driven proton acceleration by using micro-pillar arrays at high drive energy, Sci. Rep. **7,** 11366 (2017).

[31] Subhendu Kahaly, S. K. Yadav, W. M. Wang, S. Sengupta, Z. M. Sheng, A. Das, P. K. Kaw, and G. R. Kumar, Near-Complete Absorption of Intense, Ultrashort Laser Light by Sub-λ Gratings, Phys. Rev. Lett. **101,** 145001 (2008).

[32] Sudipta Mondal, Indrani Chakraborty, Saima Ahmad, Daniel Carvalho, Prashant Singh, Amit D. Lad, V. Narayanan, Pushan Ayyub, G. R. Kumar, J. Zheng, and Z. M. Sheng, Highly enhanced hard x-ray emission from oriented metal nanorod arrays excited by intense femtosecond laser pulses, Phys. Rev. B **83,** 035408 (2011).

[33] I. A. Andriyash, R. Lehe, A. Lifschitz, C. Thaury, J.-M. Rax, K. Krushelnick, and V. Malka, An ultracompact x-ray source based on a laser-plasma undulator, Nat. Commun. **5,** 4736 (2014).

[34] Shiyi Zhou, Yafeng Bai, Ye Tian, Haiyi Sun, Lihua Cao, and Jiansheng Liu, Self-Organized Kilotesla Magnetic-Tube Array in an Expanding Spherical Plasma Irradiated by kHz Femtosecond Laser Pulses, Phys. Rev. Lett. **121,** 255002 (2018).

[35] Sudipta Mondal, Hassan A. Hafez, Xavier Ropagnol, and Tsuneyuki Ozaki, MV/cm terahertz pulses from relativistic laser-plasma interaction characterized by nonlinear terahertz absorption bleaching in *n*-doped InGaAs, Opt. Express **25,** 17511 (2017).

[36] M. Thévenet, H. Vincenti, and J. Faure, On the physics of electron ejection from laser-irradiated overdense plasmas, Phys. Plasmas **23,** 063119 (2016).

[37] R. Pompili, M. P. Anania, F. Bisesto, M. Botton, M. Castellano, E. Chiadroni, A. Cianchi, A. Curcio, M. Ferrario, M. Galletti, Z. Henis, M. Petrarca, E. Schleifer, and

A. Zigler, Femtosecond dynamics of energetic electrons in high intensity laser-matter interactions, Sci. Rep. **6,** 35000 (2016).

[38] Prashant Kumar Singh, Y. Q. Cui, Gourab Chatterjee, Amitava Adak, W. M. Wang, Saima Ahmed, Amit D. Lad, Z. M. Sheng, and G. Ravindra Kumar, Direct observation of ultrafast surface transport of laser-driven fast electrons in a solid target, Phys. Plasmas **20,** 110701 (2013).

[39] B. Dromey, S. Rykovanov, M. Yeung, R. Hörlein, D. Jung, D. C. Gautier, T. Dzelzainis, D. Kiefer, S. Palaniyppan, R. Shah, J. Schreiber, H. Ruhl, J. C. Fernandez, C. L. S. Lewis, M. Zepf, and B. M. Hegelich, Coherent synchrotron emission from electron nanobunches formed in relativistic laser-plasma interactions, Nat. Phys. **8,** 804 (2012).

[40] Y. T. Li, J. Zhang, L. M. Chen, Y. F. Mu, T. J. Liang, Z. Y. Wei, Q. L. Dong, Z. L. Chen, H. Teng, S. T. Chun-Yu, W. M. Jiang, Z. J. Zheng, and X. W. Tang, Hot electrons in the interaction of femtosecond laser pulses with foil targets at a moderate laser intensity, Phys. Rev. E **64,** 046407 (2001).

[41] Aghapi G. Mordovanakis, James Easter, Natalia Naumova, Konstantin Popov, Paul-Edouard Masson-Laborde, Bixue Hou, Igor Sokolov, Gérard Mourou, Igor V. Glazyrin, Wojciech Rozmus, Valery Bychenkov, John Nees, and Karl Krushelnick, Quasimonoenergetic Electron Beams with Relativistic Energies and Ultrashort Duration from Laser-Solid Interactions at 0.5 kHz, Phys. Rev. Lett. **103,** 235001 (2009).

[42] Z. Jin, H. B. Zhuo, T. Nakazawa, J. H. Shin, S. Wakamatsu, N. Yugami, T. Hosokai, D. B. Zou, M. Y. Yu, Z. M. Sheng, and R. Kodama, Highly efficient terahertz radiation from a thin foil irradiated by a high-contrast laser pulse, Phys. Rev. E **94,** 033206 (2016).

[43] W. J. Ding and Z. M. Sheng, Sub GV/cm terahertz radiation from relativistic laser-solid interactions via coherent transition radiation, Phys. Rev. E **93,** 063204 (2016).

[44] Guo-Qian Liao, Yu-tong Li, Yi-Hang Zhang, Hao Liu, Xu-Lei Ge, Sus Yang, Wen-Qing Wei, Xiao-Hui Yuan, Yan-Qing Deng, Bao-Jun Zhu, Zhe Zhang, Wei-Min Wang, Zheng-Ming Sheng, Li-Ming Chen, Xin Lu, Jing-Long Ma, Xuan Wang, and Jie Zhang, Demonstration of Coherent Terahertz Transition Radiation from Relativistic Laser-Solid Interactions, Phys. Rev. Lett. **116,** 205003 (2016).

[45] C. B. Schroeder, E. Esarey, J. van Tilborg, and W. P. Leemans, Theory of coherent transition radiation generated at a plasma-vacuum interface, Phys. Rev. E **69,** 016501 (2004).

[46] M. Thévenet, A. Leblanc, S. Kahaly *et al.,* Vacuum laser acceleration of relativistic electrons using plasma mirror injectors, Nature Phys. **12,** 355 (2016).

[47] Susan L. Dexheimer, *Terahertz Spectroscopy: Principles and Applications* (CRC Press, Taylor & Francis Group, New York, 2007).

[48] Q. Wu and X. C. Zhang, Free-space electro-optic sampling of terahertz beams, Appl. Phys. Lett. **67,** 3523 (1995).

[49] Ajay Nahata, David H. Auston, Tony F. Heinz, and Chengjiu Wu, Coherent detection of freely propagating terahertz radiation by electro-optic sampling, Appl. Phys. Lett. **68,** 150 (1996).

[50] Yasuo Minami, Yusuke Hayashi, Jun Takeda, and Ikufumi Katayama, Single-shot measurement of a terahertz electric-field waveform using a reflective echelon mirror, Appl. Phys. Lett. **103**, 051103 (2013).

[51] K. Y. Kim, B. Yellampalle, G. Rodriguez, R. D. Averitt, A. J. Taylor, and J. H. Glownia, Single-shot, interferometric, high-resolution, terahertz field diagnostic, Appl. Phys. Lett. **88**, 041123 (2006).

[52] Jie Shan, Aniruddha S. Weling, Ernst Knoesel, Ludwig Bartels, Mischa Bonn, Ajay Nahata, Georg A. Reider, and Tony F. Heinz, Single-shot measurement of terahertz electromagnetic pulses by use of electro-optic sampling, Opt. Lett. **25**, 426 (2000).

[53] Andrea Sgattoni, Luca Fedeli, Stefano Sinigardi, Alberto Marocchino, Andrea Macchi, Volker Weinberg, and Anupam Karmakar, Optimising PICCANTE—an open source particle-in-cell code for advanced simulations on tier-0 systems, arXiv:1503.02464 (2015).

[54] J.-L. Dubois, F. Lubrano-Lavaderci, D. Raffestin, J. Ribolzi, J. Gazave, A. Compant La Fontaine, E. d'Humières, S. Hulin, Ph. Nicolaï, A. Poyé, and V. T. Tikhonchuk, Target charging in short-pulse-laser–plasma experiments, Phys. Rev. E **89**, 013102 (2014).